nature communications

Article

https://doi.org/10.1038/s41467-024-53592-9

# Local adaptive insulation in amorphous powder cores with low core loss and high DC bias via ultrasonic rheomolding

Received: 24 August 2023

Accepted: 16 October 2024

Published online: 04 November 2024

Check for updates

H. Z. Li[1], Y. Q. Yan[2], W. S. Cai[1], L. Y. Li[3], A. Yan[1], L. H. Liu[1], J. Ma[3] ✉, H. B. Ke[2], Q. Li[4], B. A. Sun[2,5] ✉, W. H. Wang[2,5] & C. Yang[1] ✉

Amorphous powder cores are promising components for next-generation power electronics. However, they present inherent challenges of internal air gaps and stresses during cold compaction, which significantly deteriorate soft magnetic properties. Here, we report the formation of a local adaptive insulation structure of biconcave lens in amorphous powder cores by ultrasonic rheomolding. Consequently, compared with conventional cold-compacted powder cores, the ultrasonic rheomolded powder cores offer significant simultaneous improvements in the permeability from 31.3–32.4 to 41.8–43.3 and the direct-current bias performance from 69.4–69.7% to 87.4–87.8% (7960 A/m), thereby overcoming the trade-off between permeability and direct-current bias performance. In particular, their core losses are as low as 13.73–15.45 kW/m$^3$, approximately one twentieth of that of the cold-compacted powder cores (282.84–304.03 kW/m$^3$) at a magnetic field of 100 mT and 100 kHz. The biconcave-lens insulation structure can effectively buffer the impact of high mechanical stress on the magnetization of magnetic powder particles, allowing for the ultrasonic rheomolded powder cores to maintain better magnetization efficiency and consequently resulting in excellent soft magnetic properties under the cooperative effect of very low internal stresses and low porosity. The ultrasonic rheomolded powder cores can be used as alternative core components in next generation miniaturized power electronics.

With the development of the electric power industry, electronics are needed to meet the requirements of miniaturization, high frequency, and high current[1–4]. Powder cores (PCs) are widely used in electronics as vital components of transformers and inductors[1,5]. In fact, approximately 9% of the electricity is lost during transmission and distribution, and a significant portion of these losses can be attributed to the magnetic component of power converters such as PCs[6]. Achieving excellent comprehensive performance with high permeability, low energy loss, and high direct-current (DC) bias performance of PCs is highly desirable for improving transmission efficiency[7,8].

Today, Fe-based amorphous PCs are one of the choices for electronics due to their excellent overall magnetic properties[9,10]. They are generally fabricated by compacting and annealing insulation-coated amorphous alloy powders[9–12]. Currently, research aimed at enhancing

[1]National Engineering Research Center of Near-net-shape Forming for Metallic Materials, Guangdong Provincial Key Laboratory for Processing and Forming of Advanced Metallic Materials, South China University of Technology, Guangzhou, China. [2]Songshan Lake Materials Laboratory, Dongguan, China. [3]Guangdong Provincial Key Laboratory of Micro/Nano Optomechatronics Engineering, Shenzhen University, Shenzhen, China. [4]State Key Laboratory of Advanced Materials and Electronic Components, Guangdong Fenghua Advaced Technology Holding CO., LTD, Zhaoqing, China. [5]Institute of Physics, Chinese Academy of Sciences, Beijing, China. ✉e-mail: majiang@szu.edu.cn; Sunba@iphy.ac.cn; cyang@scut.edu.cn

https://doi.org/10.1038/s41467-024-53592-9

the performances of Fe-based amorphous PCs often employs two strategies. One is to design and develop new compositions of amorphous powders, such as Finemet[13], $Fe_{76}Si_9B_{10}P_5$[14], and $Fe_{85.5}B_{10}Si_2P_2C_{0.5}$[15], which have high magnetic saturation ($B_s$) and low coercivity ($H_c$). Another is to tailor the physical and chemical properties of the insulation layers, which are evenly distributed on the surface of magnetic powder particles. One example is the regulation of the resin content[10,16] and the use of $SiO_2$ insulation layers by the sol-gel method which has gained popularity in recent years[12]. However, both approaches for optimizing PCs encounter two challenges: a significant presence of internal air gaps and a large amount of internal stress. The presence of internal air gaps is attributed to the inferior deformability of amorphous powders, which frequently weakens the magnetic coupling between powder particles. Moreover, the low annealing temperature, constrained by the amorphous crystallization temperature, presents a challenge in alleviating the significant internal stress generated during cold compaction (approximately 1800 MPa). These internal stress contributes to the degradation of the soft magnetic properties of the resultant PCs. Therefore, exploring methods to minimize the influence of internal air gaps and internal stress and achieve the molding of high-density PCs under low pressure is a valuable research direction.

Regarding soft magnetic performance, there is a trade-off relationship between the permeability and the DC bias performance in PCs[10,12,17–19]. Generally, the insulation layer is critical for these properties. An increase in the thickness of the insulation layer results in a decrease in the permeability while simultaneously leading to an increase in the DC bias performance. An increase in the amount of nonmagnetic per unit area decreases the magnetic content and permeability[10]. Furthermore, a dense insulation layer reduces the magnetic induction on the powder, boosting the DC bias performance [12,17]. Therefore, overcoming this trade-off relationship and achieving excellent comprehensive magnetic properties for Fe-based amorphous PCs has become a major challenge.

To address these issues, in this work, we report an ultrasonic rheomolding (UR) strategy to develop PCs that effectively improve the problem of weakened magnetic coupling resulting from the presence of air gaps and a large amount of internal stress. Additionally, this approach breaks the trade-off relationship between the permeability and DC bias performance internally. Using commercial Kuamet 6B2 amorphous powder as the raw material, the permeability of the URPCs increased by 32–34%, and the corresponding DC bias performance increased from 69.4–69.7% to 87.4–87.8% (7960 A/m) compared to those of the conventional cold-compacted PCs. The resolution of this trade-off is attributed to the so-called local adaptive insulation structure of the biconcave lens in the URPCs, which can effectively buffer the impact of high mechanical stress on the magnetization of magnetic powder particles, allowing for the URPCs to maintain better magnetization efficiency. Equally importantly, the corresponding core loss of the URPCs can be reduced to about one-twentieth, from 282.84–304.03 $kW/m^3$ to 13.73–15.45 $kW/m^3$ at 100 mT and 100 kHz, representing a large breakthrough in amorphous PCs. In addition, the molding pressure applied for the URPCs can be decreased to 6.2 MPa, which is only one three-hundredth of that used for the cold-compacted PCs (1800 MPa).

## Results

### Ultrasonic rheomolding PCs (URPCs)

The insulation resin often has a significant influence on the magnetic properties of PCs[10], even though it does not contain magnetic materials. The greater the thickness of the insulation layer, the lower the permeability of the PCs, and the greater the DC bias capacity. This is related to the reduction in magnetic powders per unit volume of PCs and the increase in the demagnetizing field[14]. In the case of PCs, the presence of internal air gaps is associated with the geometry of the insulation structure of the resin, which often weakens the magnetic coupling and leads to partial flux leakage, thereby deteriorating the permeability and core losses.

If the resin structure is controlled to aggregate near the adjacent points between powder particles, the magnetic powder surfaces can be partially exposed. Furthermore, the exposed powder surfaces can strengthen the magnetic coupling between powder particles, while the aggregated resin can also enhance the saturation resistance of the PCs. The trade-off relationship between the permeability and DC bias performance may be overcome by designing the insulation structure of the resin between adjacent amorphous powder particles.

Here, we present a insulation structure that differs from the conventional one. Its presence provides a larger contact area to buffer mechanical stress generated by magnetic force from the magnetic powder particles during magnetization. Furthermore, an uncoated structure (unaffected by mechanical stress) was used as a control group (Fig. 1c) to verify the conclusion that the reduction in mechanical stress can improve soft magnetic performance, even though such a structure does not exist.

As shown in Fig. 1a, the insulation resin in the conventional insulation structure is evenly distributed around the magnetic powder wrap. Figure 1b shows the designed biconcave-lens insulation structure. The distribution of the insulation resin exhibits the geometry of a biconcave lens between two adjacent powder particles, with the resin aggregating mainly near adjacent points of the powder particles, providing a larger contact area to buffer the mechanical stress generated. Additionally, a simulated third structure, referred to as the non-insulated structure, which is not affected by mechanical stress (Fig. 1c), was introduced and served as a control group, although such a core was not fabricated in this study. The 3D model drawings of the conventional and designed insulation structures and the analysis of the details of the designed structure are shown in Supplementary Note 1, in which the resin content (3 wt.%) and size (18 µm), and the stacking characteristics of coarse and fine magnetic powders (26 and 15 µm) and their spacing (4 µm) are the same. Furthermore, the powder spacing of the uncoated structure is also 4 µm.

To reduce magnetic leakage and improve stability, the three structures were combined and designed into a toroidal-like structure for simulation (Fig. 1d–f). All three structures had the same stacking characteristics of mismatch configuration of coarse and fine powder particles together with the different models of insulation structures. Ansys simulation indicated that at the same applied magnetic intensity of $H = 79.6$ A/m to the three coils (Fig. 1d–f), the three PCs exhibited different distributions of magnetic induction intensity ($B$) (Fig. 1g–i). Interestingly, the biconcave-lens insulation structure (Fig. 1h) allows more resin aggregation concentrated near the magnetic powder particles, thereby improving the magnetic properties of the URPCs compared to those of the conventional insulation structure. This is evidenced by the higher $B$ in Fig. 1h. Furthermore, the fully exposed magnetic particle structure (uncoated structure) shows the highest $B$ (Fig. 1i). Therefore, the biconcave-lens insulation structure has a higher $B$, indicating its higher magnetization efficiency at the same magnetic field (Supplementary Fig. 1)[1].

To prepare PCs with biconcave-lens-like insulation structures, a new process, the so-called UR process, was designed to mold amorphous alloy powder. Figure 1j shows the preparation process flow of the conventional cold-compacted (gray area) and designed UR (green area). Compared with the conventional long process of soaking, stirring, drying, sieving, cold compacting (1800 MPa), and annealing, the UR is a short process that includes only three simple steps mixing, rheomolding (6.2 MPa), and annealing. Essentially, the ultrasonic vibration transfers energy to the mixed magnetic and resin powders, resulting in the aforementioned local adaptive insulation. Specifically, the vibration of the mixed powders is generated through the high frequency vibration (20,000 Hz) of an ultrasonic punch. This causes

https://doi.org/10.1038/s41467-024-53592-9

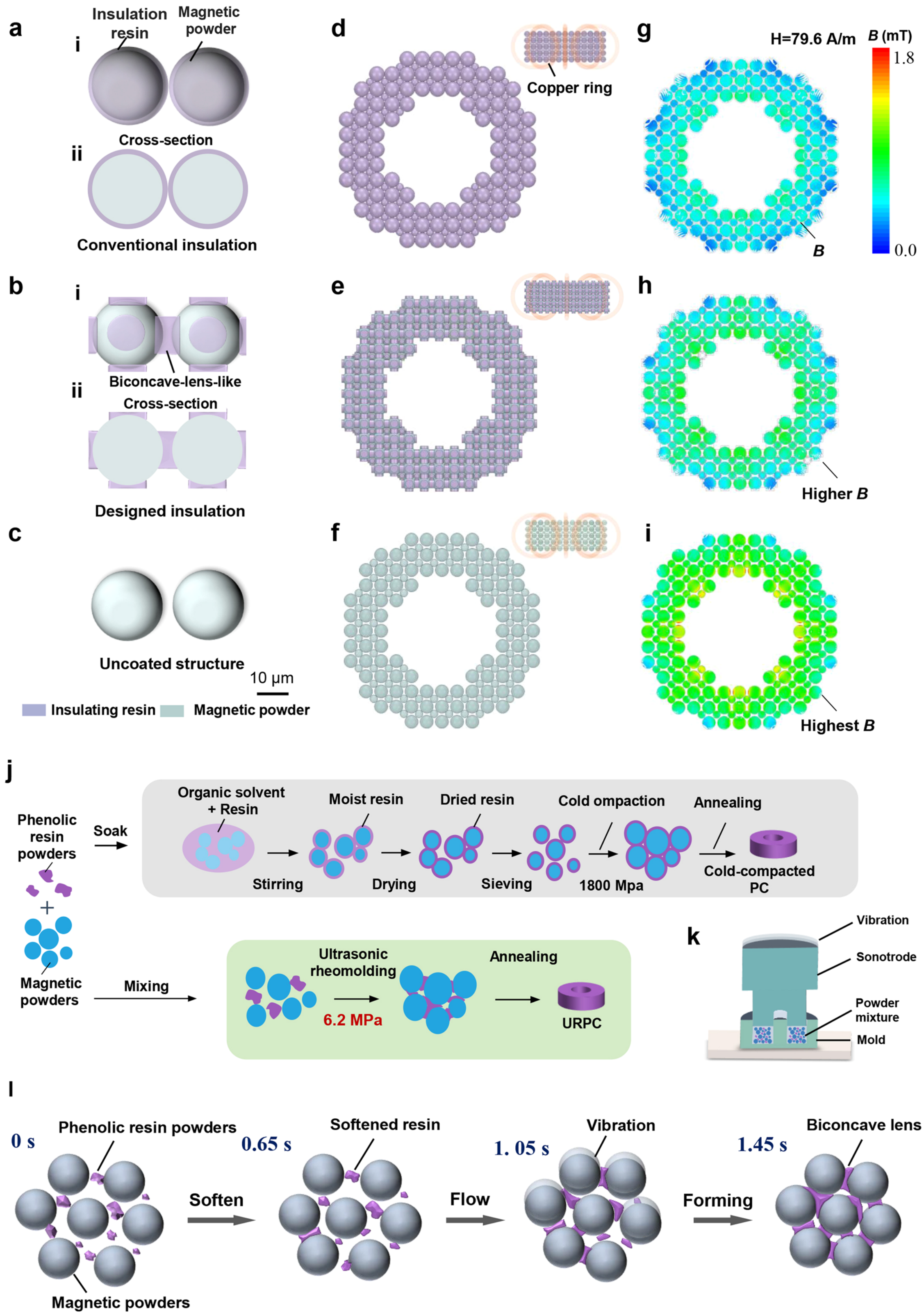


**Fig. 1 | Ansys simulation and process flow for the designed ultrasonic rheomolding powder cores (URPCs) and conventional cold-compacted PCs.** Models of the conventional insulation structure (**a**), Designed biconcave-lens insulation structure (**b**), and uncoated structure (**c**). **d**–**f** Corresponding toroidal structures of the models in (**a**–**c**), respectively. The insets show these structures consist of five layers of powder particles, in which coarse powder particles (26 μm) are interspersed with fine ones (15 μm), and the copper wires have eight winding turns. **g**–**i**, Magnetic induction intensity ($B$) generated at a magnetic field intensity of 79.6 A/m by the three coils in (**d**–**f**). **j** Schematic diagrams of the process flow for the two PCs. **k** Schematic diagram of the preparation of the URPCs. **l** Schematic diagram of the resin change process during UR.

the resin powders to absorb ultrasonic energy, soften, and subsequently flow between magnetic powder particles. Once the flowing resin is adaptively captured between two adjacent powder particles under ultrasonic vibration, a biconcave-lens-like insulation structure is formed, which is referred to as the local adaptive insulation structure of biconcave lens (Fig. 1b). Compared with that of the conventional insulation layer, its insulation layer near the area between two adjacent powder particles is thicker. Figure 1k shows a schematic diagram of UR involving the ultrasonic vibrations of the mixed amorphous alloy and resin powders, which are packaged in a toroidal groove mold and vibrated by a sonotrode. A corresponding schematic diagram of the LAI process during the UR is shown in Fig. 1l. The softening and flow of the resin powders and the vibration of the alloy powders are coupled with the preferential distribution of the resin powders, resulting in the formation of the local adaptive insulation structure of the biconcave lens as well as highly dense PCs.

### Molding mechanism and characterization of URPCs

To verify the designed insulation structure and corresponding URPCs, commercial powders of Kuamet6B2 amorphous alloy ($Fe_{73.7}Si_{11}B_{11}C_2Cr_{2.3}$, Hachinohe) and phenolic resin (18 μm, Yiyuan Plastic Chemical Material Co., Ltd) were used as raw materials. The as-received Kuamet6B2 powders exhibited a spherical shape, with an average powder size of approximately 21 μm, and a crystallization temperature of 554 °C (Supplementary Fig. 2). The maximum pressure applied during UR was as low as 6.2 MPa, with a duration of 1.5 s (Fig. 2a). Notably, the pressure is only 0.34% of that used in the conventional cold-compaction molding of PCs (1800 MPa). The very low pressure herein is a satisfactory way to solve the problem faced by conventional PCs, i.e., the low annealing temperature makes it difficult to eliminate the large number of internal stresses caused by high-pressure molding. Moreover, the maximum temperature generated by sonication is only 183 °C in UR (Supplementary Fig. 3), which does not affect the magnetic powders. Furthermore, the XRD patterns of the URPCs and cold-compacted PCs indicate that both PCs retain their amorphous-nanocrystalline structures (Fig. 2b), which is evidenced by the weak diffraction peak of α-Fe at 45°.

Figure 2c shows the FTIR spectra of the as-received amorphous powder, the mixed resin and amorphous powders, and the URPCs. It is apparent that the URPCs and mixed powders show almost the same absorption peaks at approximately 464 and 1133 $cm^{-1}$, which are associated with the Si–O–Si stretching vibration, and approximately 1633 and 3444 $cm^{-1}$, which are related to the O–H stretching vibration[20–23].

To visualize the UR process under low pressure, a high-speed camera was used to photograph the rheomolding process of the mixed amorphous and resin powders (Supplementary Video 1 and Fig. 2d). Note that the white, dark, and gray contrasts represent the amorphous and resin powders and their powder mixtures, respectively. At 0 s, the vibrational density of the mixed powders was 4.24 $g/cm^3$, corresponding to the gray contrast of the mixed powders. Basically, the resin flow and the alloy powder vibration are dominant mechanisms during UR and the resultant densification. With the loading of ultrasonic energy from 0 to 0.65 s (Fig. 2d), the resin gradually softened and thus began to flow partially and disperse adaptively, resulting in an increase in the density and the area of dark contrast. As time progressed to 0.92 s, the resin flow was significantly accelerated and the corresponding adaptive distribution was more apparent, causing the appearance of a mass of black mists marked by the yellow dashed lines.

During the subsequent period from 1.05 to 1.5 s, the resin flow continued to persist, accompanied by the remarkable high-frequency vibration of the alloy powders induced by the ultrasonic punch. These two aspects allow for the resin flowability to reach a maximum and thus facilitate the formation of high dense PCs at the low pressure of UR. Finally, at 1.5 s, the forming and corresponding coating process was completed, achieving a higher density of PCs, together with the essential dark contrast of the resin. Figure 2e–j shows SEM images of the URPCs and cold-compacted PCs. Evidently, the two powder precursors exhibit different morphologies. Compared with a spherical resin layer wrapping a single alloy powder in the conventional insulation structure (Fig. 2e and Supplementary Fig. 4), the powder precursor used in UR is a simple mixture with phenolic resin powders distributed uniformly among the amorphous alloy powders (Fig. 2f). Owing to the insulation of the resin, some fine resin powders are not obvious, as indicated by the short yellow arrows.

To demonstrate the mechanism of the resin flow and the resultant wrapping process of local adaptive insulation during UR, Fig. 2g–j shows SEM images of the cold-compacted PCs and URPCs. For the conventional cold-compacted PCs (Fig. 2g), the resin insulation layer is distributed homogeneously, similar to that in Fig. 1a, and its average thickness is approximately 420 nm without a large deviation. Interestingly, the resin wrapping layer of the URPCs exhibits the local adaptive insulation structure of biconcave lens (Fig. 2h), similar to that in Fig. 1b, which results from the above adaptive capture of the resin powders. Specifically, the biconcave-lens insulation layer exhibits a different thickness distribution near the local contact area between two adjacent powder particles. These different distributions provide indirect evidence for the present local adaptive insulation wrapping process of URPCs. The maximum thickness of the insulation layer in the URPC, 2200 nm, is 1680 nm greater than the corresponding one (420 nm) in the cold-compacted PCs, demonstrating the wrapping mechanism of the local adaptive insulation structure of biconcave lens. Noted that, the thicknesses observed in Fig. 2h are those of the edges of the biconcave-lens insulation structures. In fact, the distances between magnetic powder particles in the URPCs are equal to those in the cold-compacted PCs (Supplementary Fig. 6e, f). Furthermore, the local adaptive insulation structure of the biconcave lens is confirmed by SEM images of cross-sections of the two PCs (Fig. 2i, j), which are marked by yellow dashed lines. The insulation resin in the URPCs is mainly distributed near the local contact area between two adjacent powder particles (Fig. 2j), which differs from the homogeneously distributed resin in the cold-compacted PCs (Fig. 2i). Undoubtedly, the wrapping mechanism is expected to contribute to the excellent soft magnetic properties of the URPCs. Supplementary Note 2 analyzes the distribution of the local adaptive insulation structure of the biconcave lens on individual amorphous powders and the volume ratio occupied. In addition, Supplementary Fig. 5 shows low-magnification SEM images of the two PCs. It is obvious that there are lower volume fractions of pores and air gaps in the URPCs. Meanwhile, the greater surface area of the coarse powder particles is covered in the URPCs. These two aspects solidify that the URPCs have the lower porosities and volume fraction of air gaps.

### Relevant characteristics and potential applications of URPCs

Figure 3a shows the hysteresis loops of the URPCs and cold-compacted PCs. Notably, the optimal soft magnetic properties for the cold-compacted PCs were determined and selected by the varying compaction pressure and annealing temperature (Supplementary Note 3). The magnetization ($M$) of the URPCs was always greater than that of the cold-compacted PCs within an $8.0 \times 10^5$ A/m magnetic field[24,25].

Figure 3b presents histograms of the porosity ($\varphi$) and volume resistivity ($\rho_v$) of the two PCs. Compared to the 6.545% porosity of the cold-compacted PCs, the URPCs had a lower porosity of 1.158%. This lower porosity mainly arises from the high-frequency vibration and the softened flow of resin during the UR process, which allows for the powder particles to compact into a denser arrangement more easily. Additionally, the $\rho_v$ values of the URPCs are as high as 87.86 Ω.m, nearly four times greater than that (18.83 Ω*m) of the cold-compacted PCs. This result demonstrates the superior insulation properties of the local adaptive insulation structure of the biconcave lens compared to

 https://doi.org/10.1038/s41467-024-53592-9

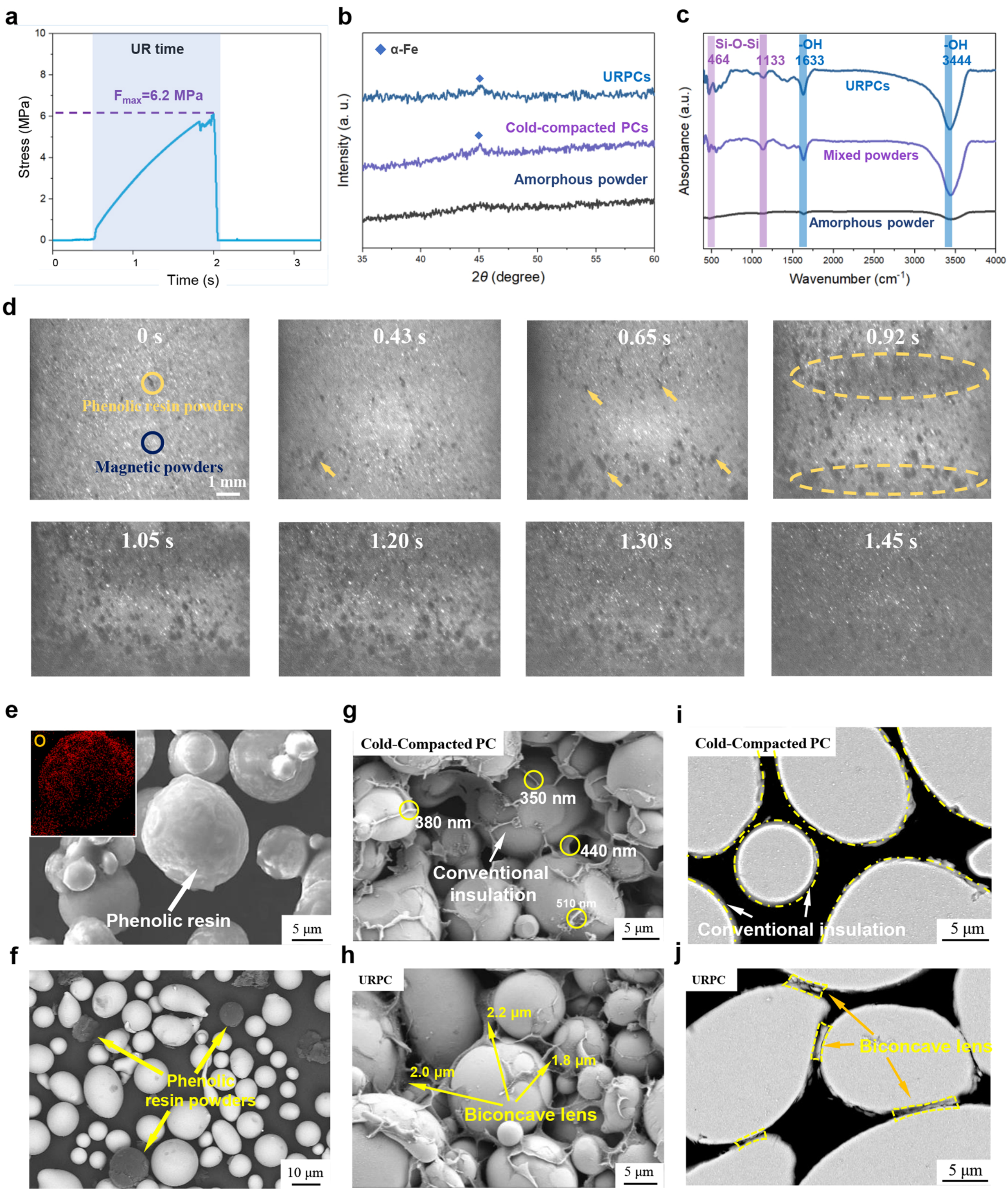


**Fig. 2 | Microstructure characterization. a** Curve of the pressure applied to the samples as a function of time during UR. The blue area indicates the time period of the UR. **b** XRD and (**c**) FTIR spectra of the as-received powder, URPCs, and cold-compacted PCs. **d** High-speed camera images of the UR process taken from Supplementary Video 1 at different times. SEM images of the resin-coated amorphous powders (**e**) and the as-fabricated (**g**) and as-sectioned (**i**) surfaces of the cold-compacted PCs, and the mixed amorphous and resin powders (**f**) and the as-fabricated (**h**) and as-sectioned (**j**) surfaces of the URPCs. The inset in (**e**) shows the surface of the powder containing visible elements including the O component (representing the resin). The yellow dashed lines in (**i**) and (**j**) indicate the types of insulation structures.

those of the conventional insulation structure. Figure 3c displays optical images of the small-size and large-size toroidal URPCs with complex geometries, which are widely used in 3 C products, indicating the feasibility of directly forming complex parts by UR.

The effective permeability ($\mu_e$) of the two PCs is shown in Fig. 3d. Although both PCs have good frequency stability from 0 to 30 MHz, the $\mu_e$ value of the URPCs, 41.8–43.3, is 34% greater than that (31.3–32.4) of the cold-compacted PCs. The improved $\mu_e$ comes from

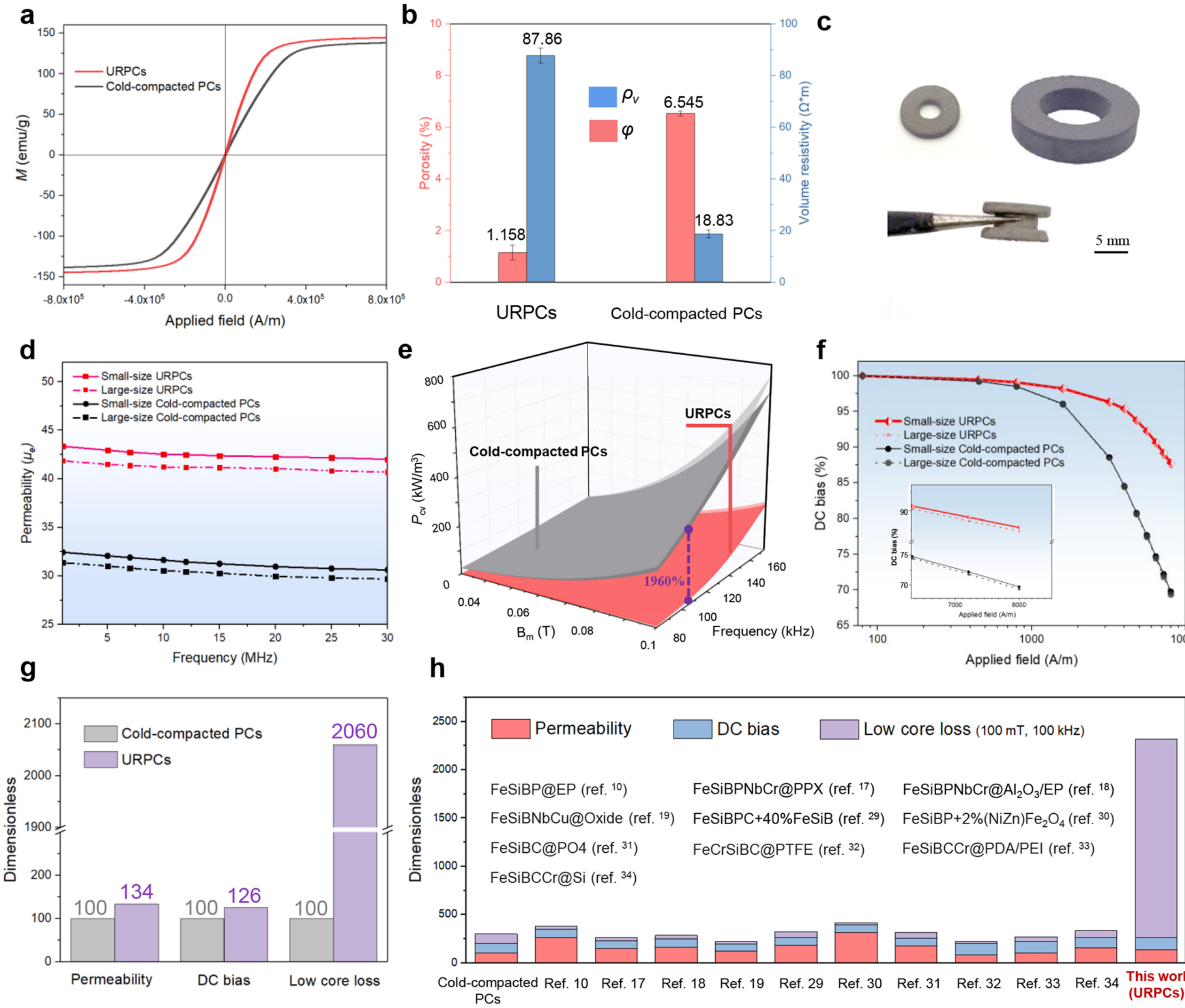


**Fig. 3 | Soft magnetic properties of the URPCs and their comparison with those of other amorphous PCs. a** Hysteresis loops of the URPCs and cold-compacted PCs. The insets show schematic diagrams of the magnetic domain structures of the two PCs. **b** Histograms of the porosity and volume resistivity of the two PCs. **c** Optical images of the small-size and large-size toroidal URPCs with complex geometries resembling the Chinese character "工". **d** Permeabilities of the two PCs with the small-size and large-size at frequencies of 1–30 MHz. **e** $P_{cv}$ of the two PCs with the small-size (non-transparent mode) and large-size (semi-transparent mode). **f** DC bias performance of the two PCs with the small-size and large-size. **g** Comparison of the soft magnetic properties of the two PCs, with values for cold-compacted PCs normalized to 100. **h** Histogram comparison of the soft magnetic properties of the URPCs and various amorphous PCs reported thus far, with the value of permeability, DC bias, and low core loss of cold-compacted PCs normalized to 100. Noted that, Although the soft magnetic properties of the large-size samples show a slight decline relative to the small-size ones in (**d**–**f**), they still maintain excellent overall performance, indicating the inapparent impact of sample size on soft magnetic properties.

several factors: the biconcave-lens insulation structure (Fig. 2h, j) enhancing the magnetization efficiency (Fig. 1h), the reduced porosity (Fig. 3b), as confirmed by Supplementary Fig. 5, and the low internal stress defects (Fig. 4b, d) due to the low pressure (Fig. 2a) in the UR[1,7]. The combination of these advantages results in a 34% increase in the $\mu_e$. Figure 3e shows the dependence of the induction and frequency on the core loss $P_{cv}$ of the two PCs. Clearly, the $P_{cv}$ value of the URPCs is always lower than that of the cold-compacted PCs at any induction and frequency. Specifically at 100 mT and 100 kHz, the $P_{cv}$ value of the URPCs is as low as 13.73–15.45 kW/m$^3$, which is approximately one twentieth of that of the cold-compacted PCs (282.84–304.03 kW/m$^3$). The detailed mechanism for the significant reduction is discussed below.

Figure 3f shows the DC bias performance of the two PCs. The mathematical definition of the DC bias is shown in Supplementary Note 4. The DC bias values (percent $\mu_e$) of the URPCs were always greater than those of the cold-compacted PCs, especially at relatively high magnetic field intensities (79.6–7960 A/m). Specifically, at 7960 A/m, the DC bias performance of the URPCs was maintained at 87.4–87.8%, which is significantly higher than that of the cold-compact PCs (69.4–69.7%). In general, an increase in the $\mu_e$ often leads to a decrease in the DC bias performance for the conventional cold-compacted PCs. Fortunately, the presence of the local adaptive insulation structure of the biconcave lens allows for the URPCs to circumvent this trade-off. Therefore, the ability to maintain $\mu_e$ at large bias currents extends the application field of magnetic devices with URPC parts[26–28]. In addition, compared to the cold-compacted PCs, the URPCs exhibited greater compressive strength (Supplementary Note 5), indicating their better bearing capacity and equivalent breakdown voltage, confirming their good reliability during the service process.

To visualize the improvement in the soft magnetic properties, Fig. 3g, h compare various property indices of the cold-compacted PC, URPC, and recently reported cold-compacted amorphous PCs with

https://doi.org/10.1038/s41467-024-53592-9

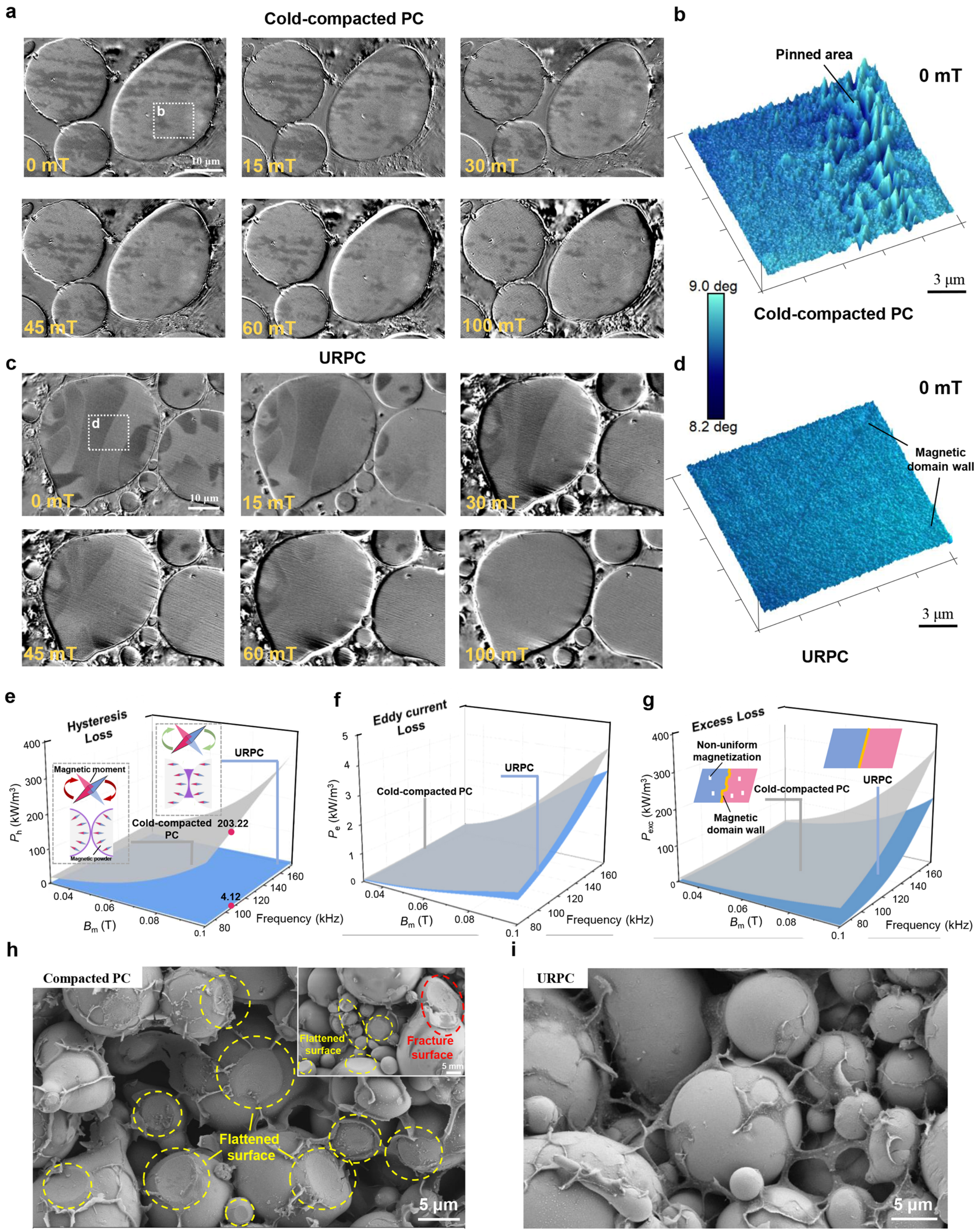


**Fig. 4 | Magnetic domain evolution, loss separation, and SEM analysis.** Magnetic domain evolution under the magneto-optical Kerr effect (MOKE) (**a**, **c**) and magnetic force microscopy (MFM) surface morphology (**b**, **d**) of the cold-compacted PCs (**a**, **b**) and ultrasonic rheomolding PCs (URPCs) (**c**, **d**). **e** Hysteresis loss, (**f**), eddy current loss, and (**g**), excess loss for the URPCs (blue) and cold-compacted PCs (gray). The insets in (**e**) show the rotation and arrangement of magnetic moments between the powder particles, with the red and green turning arrows indicating high and low resistances, respectively. The illustration in (**g**) shows diagrams of the pinning points in the magnetic domain. **h**, **i** SEM images of the cold-compacted PCs and URPCs.

various alloy compositions and insulation materials[10,17–19,29–34]. A normalization process was employed to eliminate the differences between units and magnitudes, and the method of calculation is described in Supplementary Note 6. Herein, the $\mu_e$, DC bias performance, and core loss of the cold-compacted PCs were set to 100 as a reference, and the corresponding values of the other PCs were normalized by taking the values of the cold-compacted PCs as benchmarks; the corresponding relative values for the small-size and large-size URPCs were 134, 126, and 2060, respectively, and 132, 125, and 1975, respectively, exhibiting a generalized improvement in comprehensive properties. Compared with recently reported cold-compacted amorphous PCs, the URPCs have excellent soft magnetic properties (the method of calculation is described in Supplementary Note 6), including low core loss (Fig. 3e), high DC bias performance (Fig. 3f), and high $\mu_e$ (Fig. 3d). Herein, the local adaptive insulation structure of the biconcave lens cause the URPCs to exhibit excellent soft magnetic properties.

## Discussions

To reveal the kinematic behavior of magnetic domains inside the URPCs and cold-compacted PCs, the magnetic domain evolution was observed experimentally. To eliminate the effect of compressive stress generated during polishing on magnetic domains[35,36], all the samples were polished for 3 h via vibratory polishing. Figure 4a, c show the magnetic domain evolution in the two PCs under different magnetic fields.

Both PCs exhibit uniaxial anisotropic morphologies of magnetic domains induced by a transverse magnetic field. At 0 mT, the magnetic domains in the cold-compacted PCs (Fig. 4a) presented shapes of elongated stripes and irregular clusters, while the URPCs displayed lamellar structures of magnetic domains (Fig. 4c). It follows that the large internal stresses inside the cold-compacted PCs led to the formation of massive hard-to-magnetize pinned areas, which can split the lamellar magnetic domains in the URPCs into various irregular shapes in the cold-compacted PCs. This is further evidenced by the irregular magnetic domain areas or pinned areas[37,38] in Fig. 4b and regular plane segments in Fig. 4d observed via magnetic force microscopy (MFM). The pinned areas hinder the reversal of magnetic moments and the mobility of magnetic domain walls (Fig. 4e insets). Conversely, the regular plane segments of magnetic domains in the URPCs enable easy flipping of magnetic moments and related movement of magnetic domain walls.

When the magnetic field intensity was increased to 100 mT, both PCs showed a flipping of magnetic moments (black to gray) and a movement of magnetic domains. For the cold-compacted PCs, due to the presence of pinning areas, the movement of the magnetic domains was mainly irregular (Fig. 4a). When the magnetic field was 100 mT, the cold-compacted PCs were not completely magnetized, and approximately 20% of their black magnetic domains remained unmagnetized compared to 0 mT. In contrast, the magnetic domains in the URPCs exhibited smooth movement with increasing magnetic field intensity, and the black magnetic domains were essentially fully magnetized at 100 mT compared to 0 mT.

The very low core losses of the URPCs can be explained in terms of magnetic loss separation, and the relational loss separation process is described in Supplementary Note 7. Figure 4e shows the hysteresis loss $P_h$ of the two PCs. At 100 mT and 100 KHz, the URPCs exhibited a very low hysteresis loss of 4.12 kW/m$^3$, which is only 2.0% of that (203.22 kW/m$^3$) of the cold-compacted PCs. Related analysis of coercivity can be seen in Supplementary Note 8.

For the eddy current losses $P_{\mathrm{e}}$, both PCs exhibited low losses (Fig. 4f) due to the higher powder resistivity and $\rho_\upsilon$. Due to the higher $\rho_\upsilon$ of the URPCs (Fig. 3b), $P_{inter}$ was always lower than that of the cold-compacted PCs. The excess loss $P_{exc}$ for the URPCs (Fig. 4g) is approximately 20% lower than that for the cold-compacted PCs. $P_{exc}$ is related to the nonuniform magnetization process[39,40]. Due to the significant surface collapse of the powder particles in the cold-compacted PCs under high pressure, as well as partial particle fracture (Fig. 4h), a significant amount of nonuniform magnetization regions is introduced, causing an increase in anisotropy[41]. This leads to additional energy consumption ($P_{exc}$) during the magnetization process of the PCs. The evolution of the magnetic domains in the PCs further substantiates this point. As shown in Fig. 4a, as the magnetic field was increased from 0 mT to 100 mT, the magnetization process of the cold-compacted PCs showed irregular striped magnetic domains, which introduced significant additional $P_{exc}$. In contrast, the URPCs exhibited fan-shaped large magnetic domains (Fig. 4c), allowing efficient magnetization. $P_{\mathrm{exc}}$ is due to the micro-eddy current formed around moving domain walls. Based on the MOKE images in Fig. 4a, c, it seems that the surface area of domain walls is larger in the cold-compacted PCs compared to the URPCs, and then the total $P_{\mathrm{exc}}$ would be higher in the compacted PCs.

The low value of the $P_h$ of the URPCs can be attributed to three factors: low internal stress, high densification, and a biconcave-lens-like structure. The cold-compaction molding under high pressure causes the surface of the amorphous powder to collapse, thereby introducing significant internal stress. Figure 4h shows the morphology of the cold-compacted PCs. It is clear that the amorphous powders marked by the yellow dotted box have collapsed and deformed. Furthermore, some amorphous powders fractured under high pressure as shown by the red dotted box in the inset of Fig. 4h, thereby introducing internal stress and increasing the porosity. In general, Fe-based amorphous PCs should be annealed between 570 °C and 770 °C for proper stress relief by compaction[7,41]. Therefore, at an annealing temperature of 500 °C in this work, it is difficult to relieve the significant internal stress induced by the collapse and fracturing of amorphous powders under high pressure. In contrast, the low-pressure molding of the UR, in which the resin softens and absorbs some of the stresses[5], can greatly prevent the introduction of internal stress. As shown in Fig. 4i, there is no deformation in the amorphous powder particles within the URPCs. Furthermore, the large amount of internal stress within the cold-compacted PCs is evidenced by the irregular pinned magnetic domain areas or pinned areas[37,38] in Fig. 4b. Compared to the irregular pinned areas, the regular plane segments of magnetic domains (Fig. 4d) enable easy movement of their walls, thus significantly reducing energy losses of the URPCs (Fig. 4e).

Figure 5a–d show CT images of the cold-compacted PCs and URPCs. Compared to the porosity of 6.454% for the cold-compacted PCs, the URPCs have a far lower porosity of 1.158%, indicating a significantly decreased number of pores or greater density. Fundamentally, the high porosity increases the spacing between powder particles, which weakens their magnetic coupling and thus impedes the effective rotation of magnetization vectors across the magnetic powder particles. This can decrease the effectiveness of magnetic powder particles in transmitting magnetic flux, leading to a degradation in the magnetic performance of the PCs[5,16]. Also, it can significantly increase the volume fraction of nonmagnetic materials (e.g., air), thereby decreasing the $\mu_e$[5,41]. In contrast, the low porosity of the URPCs (Fig. 5c and d) allows for the magnetic anisotropy to decrease and the free energy of the magnetic field to increase, thus favoring the rotation of the magnetization vector[16].

Finally, the enhancement in the magnetization and the reduction in the hysteresis loss of the URPCs are attributed to the biconcave-lens insulation structure, which can effectively buffer the impact of high mechanical stress on the magnetization of magnetic powder particles. During the magnetization process of the URPCs, magnetic powder particles generate either attractive or repulsive magnetic forces, which can create mechanical stress on the surface of the powder particles[42]. The presence of this stress can affect the magnetization between the powder particles, leading to a decrease in soft magnetic properties[43,44], such as the $\mu_{\mathrm{e}}$ and $P_{\mathrm{h}}$. For the conventional insulation structure, the

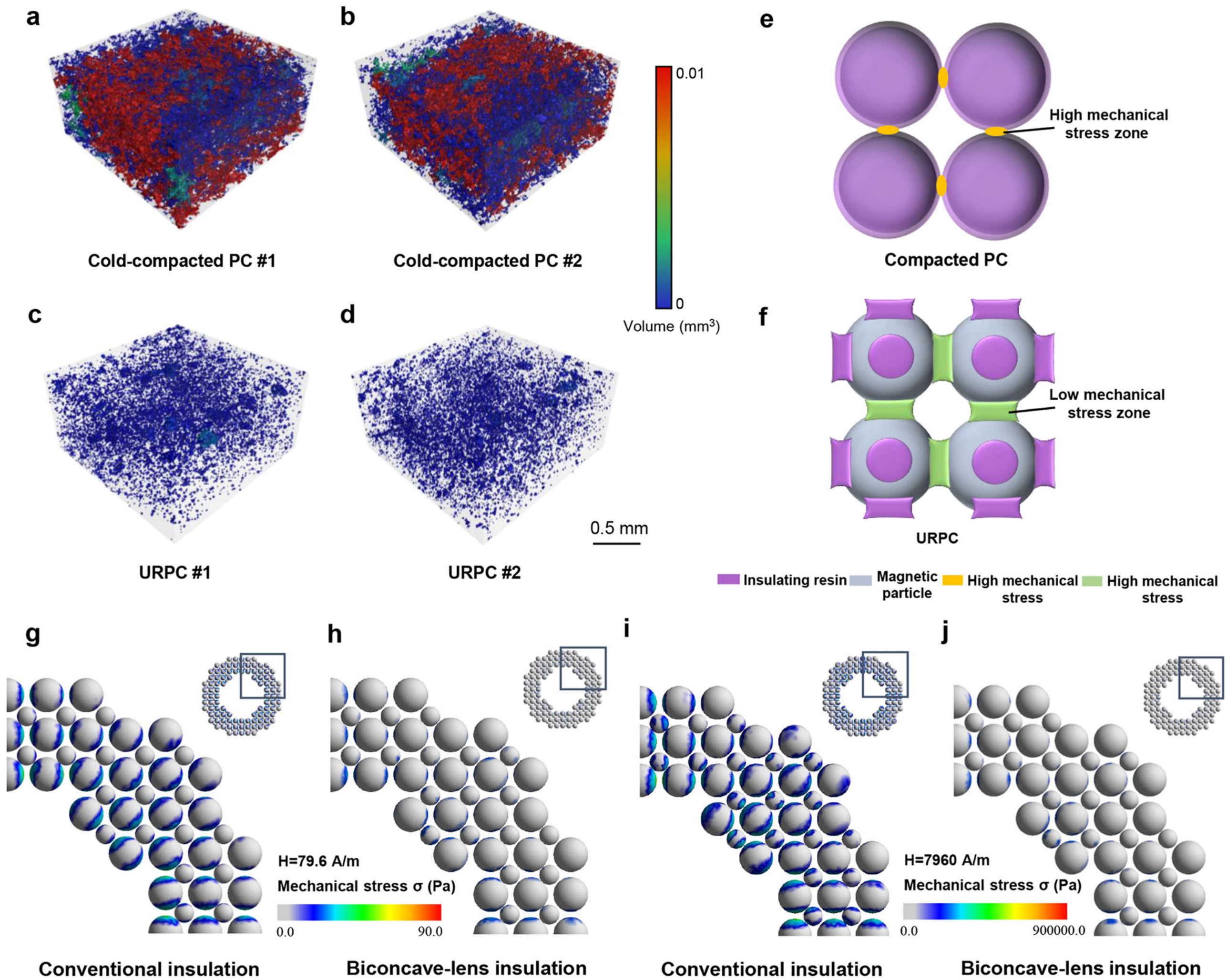


**Fig. 5 | Porosity test and mechanical stress simulation.** Computed tomography (CT) images of the cold-compacted PC samples #1 (**a**) and #2 (**b**) and URPC samples #1 (**c**) and #2 (**d**). The different colors represent different pore sizes, increasing from blue to red (see color bar on the right). Schematic diagrams of the conventional (**e**) and biconcave-lens (**f**) insulation structures used to buffer the mechanical stress generated. Mechanical stress tensor (σ) distribution of the surface layers of powder particles in the conventional (**g**, **i**) and biconcave-lens (**h**, **j**) insulation structures. To avoid the shielding effect of the insulation resin on the σ distribution, the insulation resins were removed in (**g**–**j**).

small contact area of the insulation layers between the powder particles results in a weak cushioning effect, thereby leading to a significant stress concentration (Fig. 5e). In contrast, the biconcave-lens insulation structure can provide greater area for stress buffering by the large contact area of the insulation layers between the powder particles (Fig. 5f). This can effectively reduce the effect of the mechanical stress generated by magnetic force on the magnetization of the powder particles, thus improving the soft magnetic properties of the URPCs.

Supplementary Note 9 described the distribution of the magnetic force ($F$) of magnetic powder particles, which was simulated by Ansys software. Based on the different structure models in the two insulation structures, the magnitude of the aforementioned mechanical stress received by magnetic powder particles is calculated. The corresponding mechanical stress ($\vec{\sigma}$) is calculated as[42]:

$$\vec{\sigma} = \frac{\vec{F}}{A_2} \tag{1}$$

where $A_2$ is the effective force area of the resin. Figure 5g–j shows mechanical stress tensor (σ) distribution in the two insulation structures under different magnetic field intensities. According to simulation results at a 79.6 A/m magnetic field, it is found that the conventional insulation structure presents a significantly higher stress distribution between magnetic powder particles relative to the biconcave-lens insulation structure (Fig. 5g, h).

Basically, the low-stress distribution is attributed to that the biconcave-lens insulation structure allows the resin to be distributed near the local contact area between two adjacent powder particles, significantly increasing the effective force area ($A_{2b}$) of the insulation layer and thus effectively buffering the mechanical stress generated by magnetic force between magnetic powder particles during magnetization[14,45–47], allowing for the URPCs to maintain better magnetization efficiency. Accordingly, this results in superior permeability and DC bias performance in the URPCs compared to the cold-compacted PCs (Fig. 3d, f). The lower mechanical stress generated by the magnetic force in the biconcave-lens insulation structure is confirmed under a high magnetic field intensity of 7960 A/m (Fig. 5i, j). The lower mechanical stress in the URPCs corresponds to the greater magnetic induction intensity (Fig. 1g, h) relative to the cold-compacted PCs. This allows the URPCs to maintain better magnetization efficiency, thereby inducing the higher permeability (Fig. 3d). Finally, the

DC bias, which is linearly related to the magnetization efficiency, is also improved for the URPCs (Fig. 3f).

Noted that, the 34% increase in the permeability of the URPCs relative to the cold-compacted PC is not solely attributed to the lower mechanical stress generated by magnetic force between magnetic powder particles during magnetization (Figs. 1g, h and 5g–j and Supplementary Note 9). In addition, this increase can importantly result from the introduction of low stress in the UR process (Fig. 4b, d) (molding at 6.2 MPa), and the significant reduce in the porosity from 6.454% in the cold-compacted PC to 1.158% in the URPC (Fig. 5a–d).

In summary, a local adaptive insulation structure of biconcave lens in amorphous PCs was designed using Ansys simulation and subsequently introduced via the UR method. The biconcave-lens insulation structure in the URPCs can effectively buffer the impact of high mechanical stress on the magnetization of magnetic powder particles, together with the very low internal stresses and lower porosities than those of the cold-compacted PCs. This allows for the URPCs to maintain better magnetization efficiency. Consequently, the URPCs with the biconcave-lens insulation structure exhibit simultaneous improvements in the $\mu_e$ and DC bias performance, overcoming the trade-off between the $\mu_e$ and DC bias performance. Meanwhile, the URPCs have low core losses of 13.73–15.45 kW/m$^3$ at 100 mT and 100 kHz, approximately one twentieth of that of the cold-compacted PCs. The results obtained substantiate a low-cost method for preparing high-properties URPCs for use as alternative materials in next-generation power electronics.

## Methods

### Ansys simulation

The simulations were carried out using Ansys software. The stacking configuration of the magnetic amorphous alloy powders were the same for both the conventional (Fig. 1a) and designed (Fig. 1b) insulation structures with a powder spacing of 4 µm, which is twice the thickness of the insulation layer (2 µm described below). In order to emulate actual powder stacking in PCs, stacking characteristics were optimized to be mismatch configuration of coarse and fine powders (26 and 15 µm), which is close to actual accumulation of powder particles. Meanwhile, 5 layers of powder particles were used, which can represent the effect of 50 layers of powder particles in PCs. The *B–H* lines of the magnetic powder materials represent their material properties (Supplementary Fig. 12). The conventional insulation structure has an insulation layer thickness of 2 µm, which uniformly wraps the powders. The insulation layer of the designed structure has maximum and minimum thicknesses of 6.6 and 2 µm, respectively (Supplementary Fig. 1). The phenolic insulation resins used in the two structures have equal structural volumes and have the physical properties of a polyamide material. In the simulations, the applied magnetic field intensities are 79.6 and 7960 A/m, respectively.

### Materials preparation

The as-received amorphous $Fe_{73.7}Si_{11}B_{11}C_2Cr_{2.3}$ alloy powders were produced by Epson Atmix Ltd. (Kuamet6B2, Hachinohe, Japan), and the phenolic resin powders used had a particle size of 18 µm and a softening temperature of 120 °C, and were produced by Guangdong Province Yiyuan Plastic Chemical Material Company. The two types of PCs were prepared to confirm the advantages of the URPCs. The conventional cold-compacted PC preparation process involves six steps: initial mixing of acetone solvent (50.0 wt.%), the alloy powders (48.5 wt.%), and phenolic resin powders (1.5 wt.%), drying of the mixture in a drying oven at 80 °C for 1.5 h, sieving of the dried mixture using a 160-mesh screen, the addition of 0.5 wt.% zinc stearate to the sieved mixture and stirring for 4 h, subsequent cold compaction of the stirred mixture at 1800 MPa, and final annealing of the compact at 500 °C for 0.5 h in a vacuum environment. In the above process, all procedures were carried out in a well-ventilated environment to avoid accumulation of volatile acetone. In addition, the yield in the sieving and annealing is approximately 97% and 94% on the basis of the initial alloy and phenolic resin powders, respectively.

Relative to the cold-compacted PCs, the URPCs undergo three steps: initial mixing of the blend of the alloy (97 wt.%) and phenolic resin powders (3 wt.%) together with zinc stearate (0.5 wt.%) for 4 h, subsequent molding of the mixture at a very low pressure of 6.2 MPa via UR, and final annealing of the compact at 500 °C for 0.5 h in a vacuum environment. The yield in the UR and annealing is approximately 98% and 95% on the basis of the initial blend, respectively. The dimensions of all the PCs were an outer diameter of 10 mm, an inner diameter of 4 mm, and a thickness of 1.5 mm. Noted that, these dimensions are relatively small-sizes, which are equivalent to those for various amorphous PCs products (TDK, Japan), and yet meet the requirements of miniaturization for PCs. In order to validate the effect of sample sizes particularly the thickness on soft magnetic properties, large-size PCs with 20 mm outer diameter, 12 mm inner diameter, and 4.5 mm thickness were fabricated under the same processing procedures for the small-size cold-compacted PC and URPC. Correspondingly, the vibration head of the UR was made of TC4 titanium alloy and combined with a booster and transducer to convert the electrical signal into high frequency vibration (frequency = 20,000 Hz). Therefore, the vibration head can apply mechanical vibration to the samples at low pressure. The ultrasonic energy used for molding the large-size and small-size URPCs is 850 J and 350 J, respectively. The maximum pressure during UR forming was 6.2 MPa (Fig. 2a). The vibration amplitude of the ultrasonic head was 44.4 µm.

### Characteristic analysis

The phase compositions of various PCs were characterized using an X-ray diffractometer with Cu Kα radiation (Panalytical X'pert Powder). DSC (STA449F3, Germany) was used to measure the crystallization temperature of the amorphous $Fe_{73.7}Si_{11}B_{11}C_2Cr_{2.3}$ alloy powders at a heating rate of 20 K*min$^{-1}$. SEM (Zeiss Gemini SEM300) was used to examine the morphologies of the amorphous powders and thicknesses of the insulation layers in various PCs. SEM samples were prepared by slightly grinding with 1500-grit sandpaper to further highlight the insulation layers. CT tests were performed using a German Diondo d2 device with a standard cone-beam CT scanner. The types of functional groups in the various PCs were determined by Fourier transform infrared (FTIR, Thermo Fisher Scientific Nicolet IS50-Nicolet Continuum) spectrum within the range of 400–4000 cm$^{-1}$.

### Magnetic domain detection

Magnetic domain motion with an external magnetic field was measured by a MOKE (em-Kerr-highres). To ensure that the observed magnetic domains were not affected by the compressive stress generated during polishing [36], all the samples were polished for 3 h using vibratory polishing. Prior to the measurement, a background image was collected as a reference in the AC demagnetized state. Subsequently, the images acquired at different applied fields were enhanced by subtracting the background image using KerrLab software. The evolution process of magnetic domain in the PCs was further observed by MFM (Dimension ICON with Nano Scope V controller, Bruker). For the observations, Si cantilevers coated with a Co film with the normal resonance frequency of 75 kHz and spring constant of 2.8 N*m$^{-1}$ (PPP-MFMR, Nanosensors) were used for the MFM images. The distance between the tip and PCs samples was maintained constant at 50 nm. The external magnetic field was generated by a custom electromagnet after calibration with a Hall probe. The long-range force interactions between the magnetic probe and PCs samples in the MFM were recorded and correlated in the second pass from the shift in phase from the initial driving parameters of the oscillating cantilever, which ultimately manifested as a color contrast in the images.

### Soft magnetic properties measurements

The effective permeability of various toroidal PCs was measured using an LCR meter (Agilent E4990A, Germany) in the frequency range of 1 MHz to 30 MHz. The hysteresis loops of various toroidal PCs were tested by an integrated physical property test system (PPMS-9). The resistivity of various PCs was obtained by a four-probe instrument (HPS-2526). The core loss of various toroidal PCs was calculated using a B-H analyzer (iwatsu SY-8219). The DC bias performance of various toroidal PCs was measured by a wide frequency LCR meter (TH2828A) with a DC bias current source (Agilent 42841 A). The effective permeability was calculated as follows[16]:

$$\mu_e = \frac{L \cdot l_e}{\mu_0 N^2 A_e} \tag{2}$$

where, $L$ is the inductance; $l_e$ is the effective magnetic circuit length; $N$ is the number of copper wire turns; $A_e$ is the effective cross-sectional area; and $\mu_O$ is the permeability of vacuum ($4\pi \times 10^{-7}$ H/m). For the permeability, core loss, and DC bias performance tests, the PCs were wrapped with 20 turns of copper wires.

The breakdown voltages of various PCs were tested using TH2683A insulation resistance meter system. The test voltage was started at 50 V and increased by 20 V each time. The breakdown voltage was determined when the test system displayed a short circuit. To guarantee repeatability, three samples fabricated under the same conditions were tested for all PCs.

## Data availability

The authors declare that the data supporting the findings of this study are available within the article and its Supplementary Information files. Source data are provided as a Source data file. Source data are provided with this paper.

## References


1. Silveyra, J. M., Ferrara, E., Huber, D. L. & Monson, T. C. Soft magnetic materials for a sustainable and electrified world. *Science* **362**, eaao0195 (2018).
2. Shokrollahi, H. & Janghorban, K. Soft magnetic composite materials (SMCs). *J. Mater. Process. Technol.* **189**, 1–12 (2007).
3. Herzer, G. Modern soft magnets: amorphous and nanocrystalline materials. *Acta Mater.* **61**, 718–734 (2013).
4. Svensson, L., Frogner, K., Jeppsson, P., Cedell, T. & Andersson, M. Soft magnetic moldable composites: properties and applications. *J. Magn. Magn. Mater.* **324**, 2717–2722 (2012).
5. Perigo, E. A., Weidenfeller, B., Kollár, P. & Füzer, J. Past, present, and future of soft magnetic composites. *Appl. Phys. Rev.* **5**, 031301 (2018).
6. Gutfleisch, O. et al. Magnetic materials and devices for the 21st century: stronger, lighter, and more energy efficient. *Adv. Mater.* **23**, 821–842 (2011).
7. Sunday, K. J. & Taheri, M. L. Soft magnetic composites: recent advancements in the technology. *Met. Powder Rep.* **72**, 425–429 (2017).
8. Zhao, B., Song, Q., Liu, W. & Sun, Y. Overview of dual-active-bridge isolated bidirectional DC-DC converter for high-frequency-link power-conversion system. *IEEE T. Power Electr.* **29**, 4091–4106 (2013).
9. Chang, C. et al. Improvement of soft magnetic properties of FeSiBPNb amorphous powder cores by addition of FeSi powder. *J. Alloy. Compd.* **788**, 1177–1181 (2019).
10. Chang, C. et al. Low core loss combined with high permeability for Fe-based amorphous powder cores produced by gas atomization powders. *J. Alloy. Compd.* **766**, 959–963 (2018).
11. Yagi, M. et al. Magnetic properties of Fe-based amorphous powder cores produced by a hot-pressing method. *J. Magn. Magn. Mater.* **215**, 284–287 (2000).
12. Sun, H., Wang, C., Wang, J., Yu, M. & Guo, Z. Fe-based amorphous powder cores with low core loss and high permeability fabricated using the core-shell structured magnetic flaky powders. *J. Magn. Magn. Mater.* **502**, 166548 (2020).
13. Yoshizawa, Y. A., Oguma, S. & Yamauchi, K. New Fe-based soft magnetic alloys composed of ultrafine grain structure. *J. Appl. Phys.* **64**, 6044–6046 (1988).
14. Makino, A., Kubota, T., Makabe, M., Chang, C. & Inoue, A. FeSiBP metallic glasses with high glass-forming ability and excellent magnetic properties. *Mat. Sci. Eng. B* **148**, 166–170 (2008).
15. Li, H. et al. Design of Fe-based nanocrystalline alloys with superior magnetization and manufacturability. *Mater. Today* **42**, 49–56 (2021).
16. Guo, Z. et al. Crystal-like microstructural Finemet/FeSi compound powder core with excellent soft magnetic properties and its loss separation analysis. *Mater. Des.* **192**, 108769 (2020).
17. Zhang, Y. Q. et al. Poly-para-xylylene enhanced Fe-based amorphous powder cores with improved soft magnetic properties via chemical vapor deposition. *Mater. Des.* **191**, 108650 (2020).
18. Zhang, Y. et al. High filling alumina/epoxy nanocomposite as coating layer for Fe-based amorphous powder cores with enhanced magnetic performance. *J. Mater. Sci. Mater. El* **30**, 14869–14877 (2019).
19. Kim, T., Jee, K., Kim, Y. B., Byun, D. & Han, J. High-frequency magnetic properties of soft magnetic cores based on nanocrystalline alloy powder prepared by thermal oxidation. *J. Magn. Magn. Mater.* **322**, 2423–2427 (2010).
20. Wan, J. et al. Reactivity characteristics of $SiO_2$-coated zero-valent iron nanoparticles for 2, 4-dichlorophenol degradation. *Chem. Eng. J.* **221**, 300–307 (2013).
21. Eivazzadeh-Keihan, R., Radinekiyan, F., Maleki, A., Salimi Bani, M. & Azizi, M. A new generation of star polymer: magnetic aromatic polyamides with unique microscopic flower morphology and in vitro hyperthermia of cancer therapy. *J. Mater. Sci.* **55**, 319–336 (2020).
22. Sun, K. et al. Intergranular insulating reduced iron powder-carbonyl iron powder/$SiO_2$-$Al_2O_3$ soft magnetic composites with high saturation magnetic flux density and low core loss. *J. Magn. Magn. Mater.* **493**, 165705 (2020).
23. Maleki, A. $Fe_3O_4$/$SiO_2$ nanoparticles: an efficient and magnetically recoverable nanocatalyst for the one-pot multicomponent synthesis of diazepines. *Tetrahedron* **68**, 7827–7833 (2012).
24. Kittel, C. Physical theory of ferromagnetic domains. *Rev. Mod. Phys.* **21**, 541 (1949).
25. Mohri, K., Humphrey, F., Kawashima, K., Kimura, K. & Mizutani, M. Large Barkhausen and Matteucci effects in FeCoSiB, FeCrSiB, and FeNiSiB amorphous wires. *IEEE Trans. Magn.* **26**, 1789–1791 (1990).
26. Ma, G. et al. Effects of DC bias on magnetic performance of high grades grain-oriented silicon steels. *J. Magn. Magn. Mater.* **426**, 575–579 (2017).
27. Subramanian, A. S., Meenalochini, P., Sathiya, S. S. B. & Prakash, G. R. A review on selection of soft magnetic materials for industrial drives. *Mater. Today.: Proc.* **45**, 1591–1596 (2021).
28. Kim, Y. & Zhao, X. Magnetic soft materials and robots. *Chem. Rev.* **122**, 5317–5364 (2022).
29. Wang, X. et al. New Fe-based amorphous compound powder cores with superior DC-bias properties and low loss characteristics. *J. Magn. Magn. Mater.* **324**, 2727–2730 (2012).
30. Xiao, L., Ya, D., Min, L., Chuntao, C. & Xin, W. New Fe-based amorphous soft magnetic composites with significant enhancement of magnetic properties by compositing with nano-(NiZn) $Fe_2O_4$. *J. Alloy. Compd.* **696**, 1323–1328 (2017).
31. Otsuka, I., Kadomura, T., Ishiyama, K. & Yagi, M. Magnetic properties of Fe-based amorphous powder cores with high magnetic flux density. *IEEE Trans. Magn.* **45**, 4294–4297 (2009).

32. Si, J., Ma, R., Wu, Y., Dong, Y. & Yao, K. Microstructure and magnetic properties of novel powder cores composed of iron-based amorphous alloy and PTFE. *J. Mater. Sci.* **57**, 8154–8166 (2022).
33. Huang, Y. et al. Polydopamine/polyethyleneimine enhanced Fe-based amorphous powder cores with improved magnetic properties. *J. Alloy. Compd.* **920**, 165889 (2022).
34. Liu, Y. P., Yi, Y. D., Shao, W. & Shao, Y. F. Microstructure and magnetic properties of soft magnetic powder cores of amorphous and nanocrystalline alloys. *J. Magn. Magn. Mater.* **330**, 119–133 (2013).
35. Bai, F., Li, J., Viehland, D., Wu, D. & Lograsso, A. Magnetic force microscopy investigation of domain structures in Fe–xat.% Ga single crystals (12<x<25). *J. Appl. Phys.* **98**, 2 (2005).
36. Mudivarthi, C. et al. Magnetic domain observations in Fe–Ga alloys. *J. Magn. Magn. Mater.* **322**, 2023–2026 (2010).
37. Batista, L., Rabe, U. & Hirsekorn, S. Magnetic micro-and nanostructures of unalloyed steels: domain wall interactions with cementite precipitates observed by MFM. *NDT E Int.* **57**, 58–68 (2013).
38. Wu, T.-H. et al. Relaxation of pinned domains in patterned magnetic thin films. *J. Magn. Magn. Mater.* **209**, 224–227 (2000).
39. Flohrer, S. et al. Dynamic magnetization process of nanocrystalline tape wound cores with transverse field-induced anisotropy. *Acta Mater.* **54**, 4693–4698 (2006).
40. Bertotti, G. General properties of power losses in soft ferromagnetic materials. *IEEE Trans. Magn.* **24**, 621–630 (1988).
41. Wu, C., Chen, H., Lv, H. & Yan, M. Interplay of crystallization, stress relaxation and magnetic properties for FeCuNbSiB soft magnetic composites. *J. Alloy. Compd.* **673**, 278–282 (2016).
42. Ku, J., Liu, X., Chen, H., Deng, R. & Yan, Q. Interaction between two magnetic dipoles in a uniform magnetic field. *AIP Adv.* **6**, 025004 (2016).
43. Fiorillo, F., Bertotti, G., Appino, C. & Pasquale, M. in *Wiley Encyclopedia of Electrical and Electronics Engineering*, 1–42 (*John Wiley & Sons, Inc.*, 2016).
44. Zou, P., Yu, W. & Bain, J. A. Influence of stress and texture on soft magnetic properties of thin films. *IEEE Trans. Magn.* **38**, 3501–3520 (2002).
45. Griffiths, D. J. Introduction to electrodynamics. (Cambridge University Press, 2023).
46. Luo, F. et al. Microstructure, formation mechanism and magnetic properties of $Fe_{1.82}Si_{0.18}@Al_2O_3$ soft magnetic composites. *J. Magn. Magn. Mater.* **493**, 165744 (2020).
47. Daniel, L. An analytical model for the effect of multiaxial stress on the magnetic susceptibility of ferromagnetic materials. *IEEE Trans. Magn.* **49**, 2037–2040 (2013).


## Acknowledgements

C.Y. was supported financially by the Guangdong Basic and Applied Basic Research Foundation (Nos. 2019B030302010 and 2022B1515120082), the National Natural Science Foundation of China (Nos. 52371027), and the Guangdong Science and Technology Innovation Project (No. 2021TX06C111). B.S. was supported financially by the National Natural Science Foundation of China (No. 52192602)

## Author contributions

H.L. and C.Y. conceived the work. J.M., B.S., W.W., and C.Y. supervised the work. H.L. and Y.Y. conducted the molding experiments. W.C. and L.H.L. designed the experimental setup. LY.L., Z.H., and A.Y. performed the SEM. Q.L. and J.M. performed the soft magnetic properties test. H.K. and B.S. conducted the reference investigation. H.L. carried out SEM observation, XRD, CT, mechanical properties test, and so on. H.L. and C.Y. wrote the manuscript. All authors contributed to the discussion and analyzed the results.

## Competing interests

The authors declare no competing interests.

## Additional information

**Supplementary information** The online version contains supplementary material available at https://doi.org/10.1038/s41467-024-53592-9.

**Correspondence** and requests for materials should be addressed to J. Ma, B. A. Sun or C. Yang.

**Peer review information** *Nature Communications* thanks Hasan Ahmadian Baghbaderani, Hajime Igarashi, Karthikeyan Ramachandran and the other, anonymous, reviewer(s) for their contribution to the peer review of this work. A peer review file is available.